PHYSICAL REVIEW C VOLUME 24, NUMBER 2 AUGUST 1981

# $K$ components for the ~1.4-, ~1.6-, and ~1.7-MeV structures in the fission of $^{232}$Th+$n$

G. F. Auchampaugh
*University of California, Los Alamos National Laboratory, Los Alamos, New Mexico 87545*

S. Plattard
*Service de Physique Neutronique et Nucléaire, Centre d'Etudes de Bruyères-la-Châtel, 92542 Montrouge Cedex, France*

N. W. Hill, G. de Saussure, R. B. Perez, and J. A. Harvey
*Oak Ridge National Laboratory, Oak Ridge, Tennessee 37830*

(Received 16 March 1981)

Neutron-induced angle-integrated fission cross sections of $^{232}$Th were measured from 1.3 to 1.8 MeV with a nominal neutron energy resolution of 0.15 ns/m. Data were taken for the angular intervals 0° to 23.4°, 0° to 33.7°, 0° to 51.7°, and 0° to 90°. The structure at ~1.4, ~1.6, and ~1.7 MeV were interpreted in terms of rotational bands with $K = 1/2$, 3/2, and $\geq 5/2$. The approximate relative fission strengths for the $K$ bands are in the proportion 1.7:2.4:1.0, 0.0:2.6:1.0, and 1.0:2.8:0.0 for the three structures, respectively.

[NUCLEAR REACTIONS $^{232}$Th$(n,f)$, 1.3 MeV $\leq E_n \leq$ 1.8 MeV, measured $(d\sigma_f/d\Omega)(0°-\theta_m, E_n)$ for $\theta_m$ = 23.4°, 33.7°, 51.7°, and 90°. Determined $K = \frac{1}{2}, \frac{3}{2}$, and $\geq \frac{5}{2}$ components of the structures at ~1.4, ~1.6, and ~1.7 MeV.]

## I. INTRODUCTION

The apparent "simple" structure (hereafter referred to as structure) observed in subthreshold neutron-induced fission of $^{231}$Pa, $^{230}$Th, and $^{232}$Th is well established from high-resolution fission cross-section measurements.[1-4] The lowest energy structures occur at neutron energies of ~157, ~180, ~350, and ~370 keV in $^{232}$Pa, at ~715 keV in $^{231}$Th, and at ~1.4, ~1.6, and ~1.7 MeV in $^{233}$Th. They have a full width at half maximum (FWHM) 2000 to 10 000 times greater than the spacing of the levels at the neutron separation energy in the first minimum of the multihumped fission barrier. In addition, they appear to be composed of many narrower structures (hereafter referred to as fine structure). Good examples of fine structure are the 157-keV structure, and possibly, the 370-keV structure in $^{232}$Pa. Furthermore, on a much finer energy scale, the shape of the structure or fine structure is modulated by low-amplitude structure (ultrafine structure) with a smaller spacing than that of the fine structure. This is evident in the neutron fission cross sections of $^{231}$Pa and $^{232}$Th.

Theoretical calculations, including mass-asymmetric distortions, of the fission barrier for nuclei with $N \sim 142$ by Möller[5] and Möller and Nix[6] predict, in addition to the second minimum, a shallow third minimum at a much larger deformation. Because the wave functions of the states in the third minimum must be odd or even under the parity operation on the octupole deformation parameter $\epsilon_3$,[5] the states occur in pairs with opposite parities. The separation between the states depends on the coupling between the two minima at $\pm\epsilon_3$. The rotational bands built on these states have opposite parities but the same rotational constant $A = \hbar^2/2\theta$ ($\theta$ is the moment of inertia of the nucleus at the third minimum), and the same absolute value of the decoupling parameter $a$ for the $K = \frac{1}{2}$ bands; the sign of $a$ is different for the two bands. Invoking a shallow third minimum that traps at least one vibrational state and possibly its associated rotational band can explain, at least qualitatively, the structure observed in the fission cross section in the subthreshold region.

Blons *et al.*[3] use the rotational model to interpret the fine structure at 715 keV in $^{231}$Th in terms of the members of a $K = \frac{1}{2}^-$ and a $K = \frac{1}{2}^+$ band. From a shape-fitting analysis of just their fission cross section data, they obtain $1.90 \pm 0.06$ keV for $A$ and $-2.28 \pm 0.10$ for $a$ (both parities). When Blons *et al.*[7] allow the decoupling parameter to be parity dependent and use, as well, available anisotropy data, they obtain 2 keV for $A$ and for $a$ either 1.3 ($K = \frac{1}{2}^+$) and $-1.5(\frac{1}{2}^-)$ or $-1.1(\frac{1}{2}^+)$ and $1.1(\frac{1}{2}^-)$. Boldeman *et al.*[8] recently reanalyzed these data together with all available anisotropy data and obtain 1.85 keV for $A$ and for $a - 1.1(\frac{1}{2}^+)$ and $1.1(\frac{1}{2}^-)$. Blons *et al.*[4] use the model to interpret the structure at 1.6 MeV in $^{233}$Th in terms of two $K = \frac{3}{2}$ bands with rotational constants of 2.46 and 2.73 keV.

It is tempting, therefore, to associate these small values for the rotational constant with the

third minimum. Typical values for the ground-state deformation are about 9 keV (Ref. 9) for nuclei in this mass region. For the fission isomers that occur in the second minimum of the fission barrier, Specht *et al.*[10] obtain 3.33 keV for the 4-ns $^{240}$Pu isomer and Backe *et al.*[11] obtain 3.36 keV for the 8-$\mu$s $^{239}$Pu isomer. Because the average thorium rotational constant is about 20% smaller than that for the fission isomers, a larger moment of inertia is required; consequently, the minimum occurs at a larger deformation. However, it is not clear, particularly in $^{233}$Th, whether the fine structure which is used to deduce the rotational constant is related to the members of a $K$ band or to fractionation of the vibrational state into more complex configurations.[12]

A high-resolution fission cross-section measurement delineates the structure in the cross section, but the data alone do not show unequivocally that the structure belongs either to special states in the second minimum or to vibrational-mode states in the third minimum. Additional information is needed about the character of this structure, such as its angular momentum components $K$, $J$, and parity $\pi$. A measurement of the angular distribution of the fission fragments can provide information on $K$, $J$, and sometimes $\pi$. Traditionally these measurements fall into two categories: (1) differential measurements with reasonable angular resolution but at selected energy intervals greater than the width of the fine structure and, in general, with poor resolution, or (2) integral measurements (0° to $\theta_m$) for a few limiting angles $\theta_m$ but at many energies over the fine structure with an energy resolution comparable to that used in the fission cross-section measurement.

In $^{232}$Pa below 370 keV where the fine-structure width is greater than 2.5 keV,[2] the differential angular distribution data[13,14] have a neutron energy resolution $\Delta E_n = 2$ to 40 keV. For the 715-keV structure in $^{231}$Th where the fine-structure theoretical width is about 7 keV,[3] the differential angular distribution data[15,16] have $\Delta E_n = 10$ to 36 keV. The time-of-flight (TOF) data[17] at 55° and 80° have $\Delta E_n < 10$ keV at 715 keV. In $^{233}$Th, where the structures have a width of about 70 keV, and the fine structure has a width probably less than 10 keV, the differential angular distribution data[18,19] have $\Delta E_n = 50$ to 100 keV. And finally, the TOF angle-integrated distribution data[4] for $\theta_m = 45°$ have $\Delta E_n = 2.3$ keV at 1.6 MeV.

Therefore, in all differential angular distribution measurements, with few possible exceptions,[13,17] the neutron energy resolution is much greater than the width of the fine structure. The TOF measurements have the necessary energy resolution, but because the structure is more complex than at first thought, a measurement of the anisotropy at one angle, or for a rather large angular interval, does not provide sufficient information to determine $K$, $J$, and $\pi$. However, for an even-odd fission nucleus, such data do provide information on the relative strengths of the $K = \frac{1}{2}$ vs $K > \frac{1}{2}$ components in the cross section because there are significant differences between these two angular distributions: $K = \frac{1}{2}$ distributions are peaked in the fore-aft direction relative to the beam direction whereas the $K > \frac{1}{2}$ distributions are peaked more at 90° to the beam direction.

For differential measurements that use monoenergetic neutrons from a charged-particle reaction, a further complication that arises is knowing accurately the energy of the neutron from the reaction. An error of 5 keV, which is not unrealistic for such reactions, becomes important when trying to measure the angular distribution for a fine structure with a width of just a few kilovolts or when comparing differential and fission cross-section data taken with different experimental resolution.

What is needed, therefore, is a high-energy resolution, good angular resolution, differential fission cross-section measurement. Such a measurement is virtually impossible with today's neutron intensities. However, as a compromise, we have undertaken anisotropy measurements of these isotopes at *more* than one limiting angle using the TOF technique. In this paper we describe the $^{232}$Th measurement and the analysis of the structure in the 1.3- to 1.8-MeV neutron energy region.

## II. EXPERIMENTAL DETAILS

### A. General

The neutron-induced fission cross-section and fission-fragment anisotropy measurements for $^{232}$Th were performed at the Oak Ridge National Laboratory Electron Linear Accelerator using the standard water-cooled tantalum target for neutron production. The data were taken using the TOF technique with a nominal time resolution of 0.15 ns/m. The accelerator was operated at either a pulse width of 5 ns (total data-acquisition time of ~343 h) or a pulse width of 6 ns (~190 h) at a repetition rate of 800 Hz and an average power on target of 8.5 kW.

### B. Fission detector

The fission-fragment detector, located at an average distance of 41.68 m from the neutron source, consists of a six-cell sealed gas scintil-

lator filled with a 98% He, 2% $N_2$ mixture at STP. The chamber is pumped for several days to a pressure of less than $10^{-7}$ Torr before it is filled with the gas mixture. The gas is not circulated and filtered during the measurement. The fission-fragment pulse-height distribution recorded simultaneously with the time information shows no pulse-height resolution degradation because of impurity buildup in the gas or breakdown of the molecules from alpha-particle radiation (over a period of several months).

Five of the cells contain natural thorium and one cell contains enriched uranium (93% $^{235}$U), which is used to measure the neutron spectrum. Thorium oxide is painted to an areal density of 2 mg/cm$^2$ of $^{232}$Th on both sides of a semicircular foil of titanium, 20-cm in diameter and 12.5-$\mu$m thick that is sandwiched between two 20-cm-diam, 0.5-mm-thick titanium rings. The uranium is electroplated on both sides of a 50-$\mu$m-thick stainless steel foil to an areal density of 0.5 mg/cm$^2$. Each foil is placed in the center of a cell that is optically isolated from the others by aluminum reflectors on all sides of the cell. A schematic diagram of the chamber is shown in Fig. 1. Cell 3 contains the uranium foil, and cells 4, 5, and 6 contain duraluminum grids placed over the fissionable deposits. Hexagonally packed holes machined into these grids limit the maximum angle $\theta_m$ of emission of the fission fragments with respect to the beam direction. The dimensional characteristics of the grids are given in Fig. 2.

Each cell is viewed by two XP 2020 Q, 5-cm-diam photomultiplier tubes. The tubes are supplied with quartz flat-face plates. The cell windows are made of quartz to achieve the maximum possible ultraviolet transmission from the scintillating gas to the photocathode surface of the tube. The tube is mounted in direct contact with the window and held in place by springs between the tube base assembly and the chamber.

### C. Electronics

The stop signal for a pair of tubes is derived from a quadruple coincidence between a signal from an ORTEC 934 constant fraction discriminator (CFD) that is used for time information, signals from each of the tubes, and a signal from another CFD that is used for the fission fragment energy bias. The stop signals from all cells are encoded and sent to the stop input of an EG&G TDC-100 time digitizer (TDC). The range on the TDC is adjusted to cover the neutron energy region of interest and to exclude the time region of the gamma burst. The zero flight-time channel for each cell is obtained by disconnecting all stop signals to the encoder except the one corresponding to the cell being checked and increasing the range to allow storage of the gamma burst. Also, in this way, the time drift in the electronics for each cell is periodically monitored during the measurement. This drift varied by less than a few hundred picoseconds over a period of months.

## III. DATA REDUCTION

### A. General

The TOF spectrum and fission-fragment pulse-height spectra for selected TOF windows were stored individually for each cell in a SEL 810B computer. The data were dumped to magnetic tape and the computer memory was cleared daily. In this way, we could monitor conveniently the

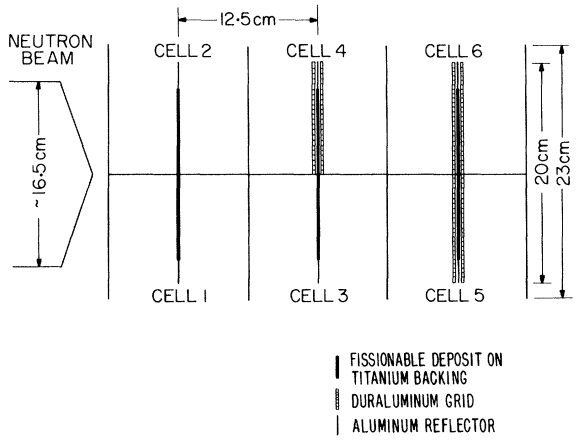


FIG. 1. Six-cell gas scintillator detector used in the neutron-induced fission cross section and anisotropy measurements of $^{232}$Th.

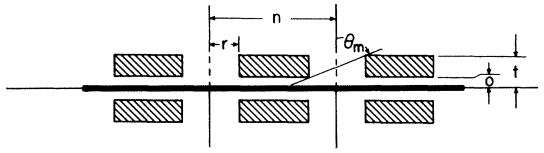


| GRID CHARACTERISTICS FOR HEXAGONALLY PACKED HOLES | | | | | |
|---|---|---|---|---|---|
| CELL (REFERENCED AS) | $\theta_m$ | r (mm) | n (mm) | o (mm) | t (mm) |
| 4 (20°) | 23·4 | 0.65 | 1.5 | 0.5 | 3.5 |
| 5 (30°) | 33.7 | 1.00 | 2.2 | 0.5 | 3.5 |
| 6 (45°) | 51.7 | 1.25 | 2 7 | 0.5 | 2.5 |

FIG. 2. Dimensional characteristics of the grids in the detector.

time drift, and time and pulse height resolution of the detector. The 5-ns burst-width data were recorded with a time/channel of 1 ns, and the 6-ns burst-width data with a time per channel of 2 ns. Because the resolution of the fine structure in the 1-ns data did not improve perceptibly over that of the 2-ns data, the 1-ns data were summed by 2 channels and added to the 2-ns data. The data from cells 1 and 2 were combined to form a single ungridded data set. All thorium data were corrected for deadtime and for a small time independent background determined from the data in the region below the fission threshold, where we expect to see essentially no neutron-induced fission events. The uranium background was obtained at low energy where $\sigma_f$ is known. The $^{235}$U data were repeatedly smoothed with a third-degree 7-point smoothing polynomial before forming ratios of the individual thorium data set to the uranium data set. And finally, the ratios were converted to cross sections using the ENDF/B-IV evaluation for the $^{235}$U fission cross section. A correction was included for the contribution of $^{238}$U(7%) to the $^{235}$U-cell data.

### B. Normalization

The $^{232}$Th fission cross section at the neutron energy $E_n$ for the $i$th cell integrated over the deposit-grid geometry (the $i$th integral fission cross section) is given by

$$\sigma_f^{232}(E_n,i) \equiv \int \frac{d\sigma_f^{232}(E_n)}{d\Omega}\, d\Omega(i) = \frac{C_i^{232}(E_n)}{C^{235}(E_n)}\, A_i \sigma_f^{235}(E_n)\,, \tag{1}$$

where $i = 20°$, 30°, 45°, and 90° (Fig. 2), $C_i^{232}$ and $C^{235}$ refer to the net counts/channel recorded for the $i$th $^{232}$Th cell and $^{235}$U cell, and $A_i$ is a normalization constant that is related to the efficiencies for detection of fission fragments and to the sample masses in the thorium and uranium cells. By choosing an energy region where the angular dependence of the fission cross section $f(\alpha)$ and the quantity $\sigma_f^{232}/\sigma_f^{235}$ are known, the normalization constant can be determined experimentally using the relation

$$A_i = \frac{\sigma_f^{232}}{\sigma_f^{235}} \frac{\sum C^{235}}{\sum C_i^{232}} \frac{W_t(i)}{2\pi}\,, \tag{2}$$

where the sum extends over all channels in the energy region, and $W_t(i) = \int f(\alpha)d\Omega(i)$ and $d\Omega(i)$ is the solid angle subtended by the $i$th grid.

The best measurement of $\sigma_f^{232}/\sigma_f^{235}$ is that of Behrens,[20] who obtains an average value of 0.127 ± 0.003 for the energy interval from 3 to 5 MeV. Lo Nigro *et al.*[21] measured the angular dependence of the fission cross section at selected energies from 1.78 to 5.23 MeV. For the energy region from 3 to 5 MeV, $f(\alpha)$ can be approximated by the even-order polynomial $0.932 + 0.205\cos^2\alpha$. The calculated values of $W_t(i)$ (Ref. 22) are $W_t(20°) = 0.109$, $W_t(30°) = 0.260$, $W_t(45°) = 0.701$, and $W_t(90°) = 2\pi$.

### C. Sample thickness effects

The average range of a fission fragment in a thorium dioxide deposit[23] is ~7.5 mg/cm$^2$. Because the thorium deposit is rather thick (2 mg/cm$^2$, which represents a significant fraction of the average range) the average maximum angle of emission of fragments from the deposit is ~82°. In the normalization of the data, this affects primarily the accuracy of the cross section for the ungridded data at energies other than in the normalization region, and only if the cross section has an energy dependent anisotropy. This can be seen by considering the correction to the cross section at an energy $E$, which is given approximately by the ratio $\int f_n(\alpha)d\Omega / \int f(\alpha,E)d\Omega$. The limits on $\alpha$ are from 0° to ~82°; the function $f(\alpha,E)$ is the anisotropy of the cross section at $E$, and $f_n(\alpha)$ is the anisotropy of the cross section in the normalization region. At $E$, this ratio is 1 if $f(\alpha,E)$ is isotropic, $<1$ if $f(\alpha,E)$ is peaked more fore-aft than in the normalization region, and $>$ if $f(\alpha,E)$ is peaked more at 90°.

We have ignored this correction because it depends on knowing the anisotropy of the cross section as a function of $E$, which is what we are trying to measure, and it affects primarily the fission cross section for which there are several high quality measurements that used rather thin deposits. However, this effect should be kept in mind when comparing our fission cross section to those measured using thinner deposits.

## IV. RESULTS

The $^{232}$Th neutron-induced angle-integrated fission cross sections in millibarns from 1.3 to 1.8 MeV for the grid angles 20°, 30°, 45°, and 90° are presented in Figs. 3–6. Statistical error bars are given every 10th data point. The curve through the data is obtained by applying a third-degree, 5-point smoothing polynomial, six times to the data. In this way, hopefully, the true structure in the data is revealed while smoothing out that from statistical fluctuations. The zero ordinate scales in Figs. 3–6 are suppressed to enhance the structure in the data. The smooth curve reveals low-amplitude structure (ultrafine structure) which occurs at all angles and has a spacing

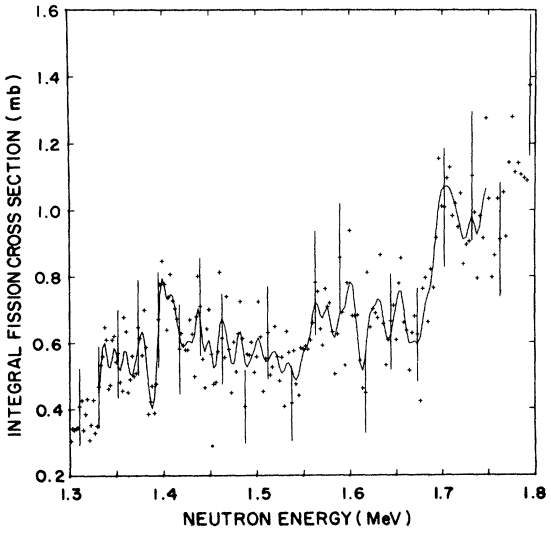


FIG. 3. Integral fission cross section for the energy interval 1.3 to 1.8 MeV for the 20° grid. The solid line is obtained from smoothing the data with a 5-point, third-degree polynomial applied six times.

of about 15 keV. Over the 1.6-MeV structure the energies of the low-amplitude structure peaks agree within 1 to 2 keV (our energy resolution at this energy is about 7 keV) with those observed in the recent high-resolution fission cross-section data presented by Blons *et al.*[7]

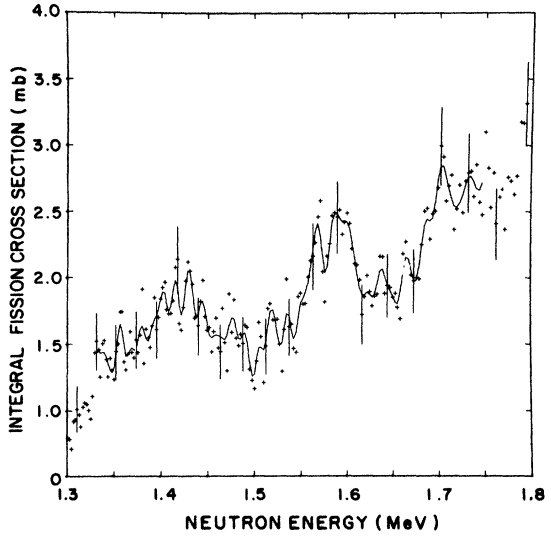


FIG. 4. Integral fission cross section for the energy interval 1.3 to 1.8 MeV for the 30° grid. The solid line is obtained from smoothing the data with a 5-point, third-degree polynomial applied six times.

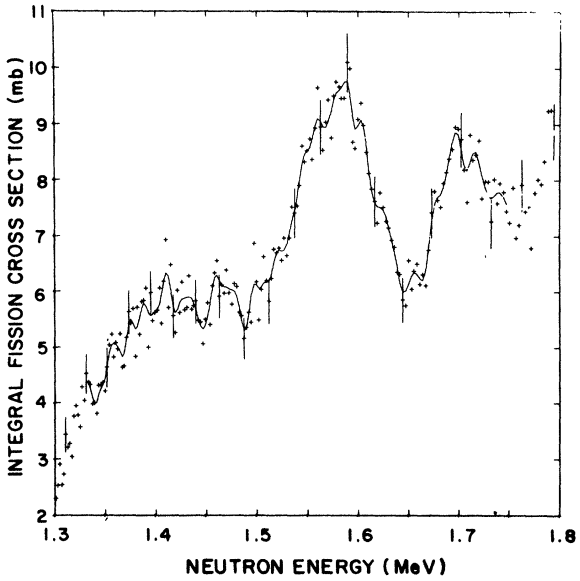


FIG. 5. Integral fission cross section for the energy interval 1.3 to 1.8 MeV for the 45° grid. The solid line is obtained from smoothing the data with a 5-point, third-degree polynomial applied six times.

## V. THEORETICAL CALCULATIONS

### A. General

Figures 3–6 show considerable structure as well as fine structure in the data at all energies. The interpretations of the structures at ~1.4,

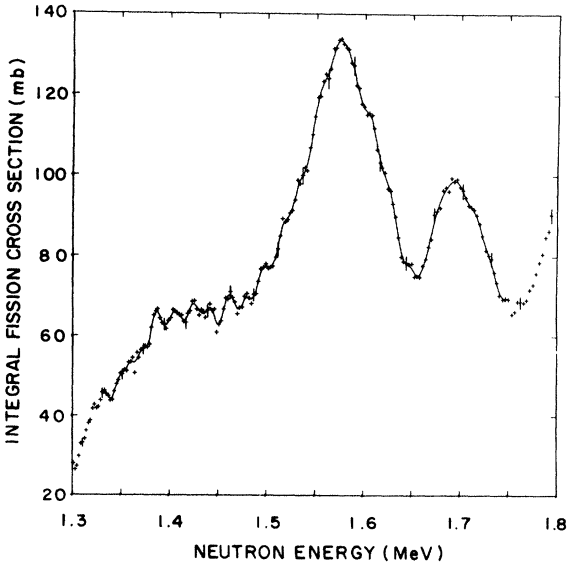


FIG. 6. Integral fission cross section for the energy interval 1.3 to 1.8 MeV for the 90° grid. The solid line is obtained from smoothing the data with a 5-point, third-degree polynomial applied six times.

~1.6, and ~1.7 MeV in $^{233}$Th by Abou Yehia *et al.*,[24] Blons *et al.*,[4] and Caruana *et al.*[18] require many $K$-vibrational states, each with a rotational band to explain, at least qualitatively, the general features in the fission cross section. The interpretation of the fine structure at 715 keV in $^{231}$Th by Blons *et al.*[3] requires two $K$ bands of opposite parity. Furthermore, numerical studies by Bjornholm and Lynn[12] of the coupling of pure vibrational states to intrinsic states at the deformation of the second minimum indicated that pure vibrational resonances are unlikely to occur in odd-mass nuclei; some observable degree of fractionation of the vibrational strength is to be expected; that is, the structures in the thorium isotopes, in particular for $^{233}$Th, may be rather complex. For these reasons, and because the statistical quality of the gridded data is poor, any detailed theoretical analysis of our data or least-square fitting of the structures is not warranted. However, it is useful to derive values for upper limits on the theoretical areas of individual $K$, $J$, $\pi$ resonances and the total area for each $K$ band (summed over all $J \geq K$ components) to compare these with the experimental areas. The area of a resonance with quantum numbers $K$, $J$, $\pi$ for angle $i$ is related to the area for angle $i'$ by just the ratio $W_t^{KJ\pi}(i')/W^{KJ\pi}(i)$ which is independent of the nuclear model chosen for the cross-section calculations. This is in contrast to the total $K$-band area which is a sum over individual $J^\pi \geq K$ components with weights that do depend on the nuclear model. However, this model dependence is weak, because for a particular $K$ the $W^{KJ}(\theta)$ functions for all $J \geq K$ (except $K = J = \frac{1}{2}$) are very similar, either forward peaked ($K = \frac{1}{2}$) or sideways peaked ($K > \frac{1}{2}$).

### B. Vibrational-resonance area

If we assume that the energy dependence of the fission cross section for a vibrational resonance located at an energy $E_{\rm vib}$ with quantum numbers $K$, $J$, $\pi$ is described by a Breit-Wigner function, then the area of the resonance is given by

$$A_t^{KJ\pi}(E_{\rm vib}, i) = (\pi/2)\sigma_f^{KJ\pi}(E_{\rm vib}, i)\Gamma_{\rm vib}^{KJ\pi},$$

where $\sigma_f^{KJ\pi}(E_{\rm vib}, i)$ is the integral fission cross section at $E_{\rm vib}$ for the grid angle $i$, and $\Gamma_{\rm vib}^{KJ\pi}$ is the FWHM of the resonance.

*Vibrational-resonance width.* To obtain an upper limit on the vibrational-resonance area $A_t^{KJ\pi}$, we need to choose a reasonable value for $\Gamma_{\rm vib}$. In $^{232}$Pa the resonance at 157 keV has an observed width of ~2.7 keV (resolution $< \frac{1}{2}$ keV).[2] The structure at ~715 keV in $^{231}$Th is composed of resonances with theoretical widths of ~7 keV.[3] In $^{233}$Th at ~1.6 MeV our 30° data suggest a resonance width of less than 10 keV if we assume that the structure, which has a total width of ~50 keV, is composed of several resonances. In our calculations, we use $\Gamma_{\rm vib} = 10$ keV for all $K$, $J$, $\pi$ resonances.

### C. Integral fission cross section

Using the Hauser-Feshbach theory[25] for compound reactions, the integral fission cross section at an energy $E_n$ for the reaction with quantum numbers $K$, $J$, $\pi$ is given by

$$\sigma_f^{KJ\pi}(E_n, i) = \frac{\sigma_{\rm CN}^{J\pi}(E_n) T_t^{KJ}(E_n) W_f^{KJ}(i) S_{n,f}}{T_N^{J\pi}(E_n) + T_\gamma^{J\pi}(E_n) + T_f^{KJ}(E_n)}, \quad (3)$$

where $\sigma_{\rm CN}^{J\pi}$ is the compound nucleus formation cross section, $T_f^{KJ}$ is the transmission coefficient for decay through the multihumped fission barrier, $T_\gamma^{J\pi}$ is the transmission coefficient for radiative decay in the ground-state well of the compound nucleus, $T_N^{J\pi}$ is the transmission coefficient for neutron decay including elastic and inelastic scattering to states in the target nucleus, $S_{n,f}$ is the level-width-fluctuation factor, which in the present calculations is taken to be unity, and $W_t^{KJ}(i) = \int f^{KJ}(\alpha) d\Omega(i)$.

#### *1. Compound-nucleus formation cross section*

The compound nucleus formation cross section in the channel-spin representation at an energy $E_n$ can be written as

$$\sigma_{\rm CN}^{J\pi}(E_n) = \pi \lambda\!\!\!^{-}_n{}^2(E_n) g(J) T_n^{ls}(E_n), \quad (4)$$

where $\lambda\!\!\!^{-}_n$ is the center-of-mass wavelength of a neutron of energy $E_n$, $g(J) = (2J+1)/2(2I+1)$, and $T_n^{ls}$ is the neutron transmission coefficient for the elastic channel with orbital angular momentum $l$ and channel spin $s$. The neutron transmission coefficient is related to the strength function $\overline{\Gamma}_n/D$ ($\overline{\Gamma}_n/D \ll 1$) in the following way:

$$T_n^{ls}(E_n) = 2\pi \overline{\Gamma}_n^{ls}/D = 4\pi \left(\frac{\gamma_n^2}{D}\right)^{ls} P^l(E_n)$$

$$= 4\pi S_n^{ls} P^l(E_n), \quad (5)$$

where $S_n^{ls}$ is the average reduced-strength function for the channel $ls$ and $P^l$ is the neutron penetrability for neutrons of orbital angular momentum $l$. For larger values of the strength function a more correct expression[26,27] for $T_n^{ls}$ is $1 - \exp(-4\pi S_n^{ls} P^l)$. This expression has the proper limiting values, namely, $T_n^{ls} = 1$ for $S_n^{ls} \gg 1$ and $T_n^{ls} = 4\pi S_n^{ls} P^l$ for $S_n^{ls} \ll 1$. In our calculations we use this form for $T_n^{ls}$ and ignore the channel-spin dependence.

Values of $\sigma_{\rm CN}^{J\pi}(E_n)$ at $E_n = 1.6$ MeV for $\frac{1}{2}^\pm \leq J^\pi \leq \frac{9}{2}^\pm$

are listed in Table I. For $S_n^{ls}$ we use 0.019 (Ref. 28) for even values of $l$ and 0.038 (Ref. 28) for odd values of $l$.

### 2. Radiative transmission coefficient

To calculate the radiative transmission coefficient, we assume that only dipole radiation contributes significantly to the radiative process. Therefore, the radiative transmission coefficient $T_\gamma^{J\pi}(E_x)$, at an excitation energy $E_x$ in the compound system $^{233}$Th, is given by

$$T_\gamma^{J\pi}(E_x) = 2\pi\bar{\Gamma}_\gamma/D = C_\gamma \int_0^{E_x} \sum_{J_f=|J-1|}^{J+1} \rho^c(E_x-\epsilon, J_f^{\pi_f})\,d\epsilon\,, \tag{6}$$

where $\rho^c(E_x - J_f^{\pi_f})$ is the level density in the compound system at an excitation energy $E_x-\epsilon$ for final states with total angular momentum $J_f$ and parity $\pi_f$, and $C_\gamma = 3.63\times10^{-7}$. The normalization constant is determined by using for slow neutron capture ($J=\frac{1}{2}^+$) in $^{232}$Th the measured values 21.2 meV and 16.7 eV (Ref. 28) for $\bar{\Gamma}_\gamma$ and $D$, respectively.

At high excitation energy, the contribution to the nuclear level density comes from combinations of nucleons independently excited from the ground state. This gives rise to the well-known independent particle level density relation

$$\rho(U,J^\pi) = \frac{(2J+1)\exp-[(2J+1)^2/8\sigma^2]}{4\sqrt{2\pi}\,\sigma^3} \times \frac{\sqrt{\pi}\exp[-2\sqrt{aU})]}{12a^{1/4}U^{5/4}}\,, \tag{7}$$

where $\sigma^2 = 0.0888aTA^{2/3}$, $T=\sqrt{U/a}$, and $a=\pi^2\rho_s/6$. The single-particle level density $\rho_s$ at the Fermi surface is given approximately by $A/12.5$. $U$ is the effective excitation energy corrected for pairing effects in the nucleus using the method proposed by Gilbert and Cameron,[29] and is given by

$$U = E_x - \epsilon - P(Z) - P(N)\,.$$

For $^{233}$Th, $P(N)=0$, $P(Z)=0.78$, and $a=31.6$ MeV$^{-1}$. In the calculations of $T_\gamma^{J\pi}$, we use this form for the level density and allow $\sigma$ to vary with energy according to the above dependence on $U$ through the nuclear temperature $T$. Values of $T_\gamma^{J\pi}(E_n)$ at $E=1.6$ MeV for $\frac{1}{2}\leq J\leq\frac{9}{2}$ are listed in Table I. We have assumed implicitly, that to first order, the nuclear level density is the same for both parities.

### 3. Total neutron transmission coefficient

The total neutron transmission coefficient for elastic and inelastic scattering to states in the residual nucleus at an excitation energy $E_x$ is given by

$$T_N^{J\pi}(E_x) = \int_0^{E_x-S_N} \sum_I \sum_{s=|I-1/2|}^{I+1/2} \sum_{l=|J-s|}^{J+s} T_n^l(\epsilon)\rho^R(E_x-S_N-\epsilon, I^\pi I)\,d\epsilon\,, \tag{8}$$

TABLE I. For the compound system $^{232}$Th + $n$, values of the compound nucleus formation cross section $\sigma_{CN}^{J\pi}(E_n)$, fission cross section $\sigma_f^{J\pi}(E_n)$ ($T_f^{kJ\pi}=1$), radiative transmission coefficient $T_\gamma^J(E_n)$, and total neutron transmission coefficient (including elastic and inelastic reactions) $T_N^{J\pi}(E_n)$, for $E_n = 1.6$ MeV.

| $J\pi$ | $T_N^{J\pi}$ | $T_\gamma^{J\pi}$ | $\sigma_{CN}^{J\pi}$ (mb) | $\sigma_f^{J\pi}$ (mb) |
|---|---|---|---|---|
| $\frac{1}{2}^+$ | 6.9 | 0.45 | 199.9 | 23.9 |
| $\frac{3}{2}^+$ | 12.0 | 0.87 | 280.3 | 20.2 |
| $\frac{5}{2}^+$ | 15.4 | 1.22 | 420.5 | 23.9 |
| $\frac{7}{2}^+$ | 16.3 | 1.48 | 78.2 | 4.16 |
| $\frac{9}{2}^+$ | 17.2 | 1.64 | 97.7 | 4.93 |
| $\frac{1}{2}^-$ | 7.8 | 0.45 | 275.8 | 29.9 |
| $\frac{3}{2}^-$ | 13.8 | 0.87 | 551.7 | 35.2 |
| $\frac{5}{2}^-$ | 16.8 | 1.22 | 389.0 | 20.5 |
| $\frac{7}{2}^-$ | 18.2 | 1.48 | 518.6 | 25.1 |
| $\frac{9}{2}^-$ | 18.1 | 1.64 | 22.8 | 1.10 |

where $\rho^R(E_x - S_N - \epsilon, I^\pi i)$ is the level density in the residual nucleus $^{232}$Th, at the excitation energy $E_x - S_N - \epsilon$; $I$ is the spin of the residual nucleus with parity $\pi_I = (-1)^I \pi$; $S_N$ is the neutron separation energy in $^{233}$Th, which is equal to 4.789 MeV.[28]

Above an excitation energy $E_x - S_N = 0.8$ MeV in the residual nucleus, $\rho^R$ is represented by the constant-temperature level density relation, $\rho^R(U) = C_n e^{-U/\theta}$, where $\theta$ is the nuclear temperature and $C_n$ is the normalization constant that is obtained from fitting the integral distribution of known levels in $^{232}$Th (Ref. 30) up to 1.6 MeV with the function

$$\frac{C_n}{2} \sum_{I=0}^{\infty} (2I+1) \exp - \left[\frac{(2I+1)^2}{8\sigma^2}\right] \int_0^{1.6} \rho^R(U)\, dU . \qquad (9)$$

The constant $\frac{1}{2}$ implies that both parities contribute equally to the level density. For $\theta = 0.58$ MeV and $\sigma = 5.3$ (Ref. 27), $C_n = 0.211$. Below $E_x = 0.8$ MeV, discrete levels in $^{232}$Th are used to preserve the known spin and parity of these levels.

Values of $T_N^{J\pi}(E_n)$ at $E_n = 1.6$ MeV for $\frac{1}{2}^{\pm} \leq J^\pi \leq \frac{9}{2}^{\pm}$ are listed in Table I.

#### 4. *Fission transmission coefficients*

Calculations of fission barriers[5,6] for the protactinium and thorium isotopes show that the inner barrier is lower than the outer barrier, and furthermore, that the outer barrier is split into two barriers separated by a shallow minimum. In fact, the inner barrier height may lie below the neutron separation energy. Consequently, if we are interested only in the properties of the states trapped in this shallow well, then the effect of the inner barrier on these properties is minimal. Therefore, we can replace the triple-humped barrier by a double-humped barrier.

The energy dependence of the penetrability or transmission coefficient through a double-humped potential represented by two inverted parabolas connected smoothly to a third parabola can be calculated exactly using the wave equation[31] or approximately using the WKB method.[32]

Using the WKB approximation, the relations between the fission barrier parameters and the vibrational resonance parameters are

$$T_{f,\max}(E_{\text{vib}}) = \frac{4 T_B T_C}{(T_B + T_C)^2} , \qquad (10a)$$

$$\Gamma_{\text{vib}} = \frac{\hbar\omega_{III}}{2\pi} (T_B T_C) , \qquad (10b)$$

$$E_{\text{vib}} = E_{III} + \hbar\omega_{III}(n + \tfrac{1}{2}), n = 0, 1, 2, \ldots , \qquad (10c)$$

and

$$T_{B,C} = 1 \Big/ \left\{ 1 + \exp\left[ \frac{2\pi}{\hbar\omega_{B,C}} (E_{B,C} - E_{\text{vib}}) \right] \right\} , \qquad (10d)$$

where $E_B, E_C$ are the inner and outer barrier heights, and $E_{III}$ the depth of the intermediate well, and $\hbar\omega_B$, $\hbar\omega_C$, and $\hbar\omega_{III}$ are the barrier curvatures. Therefore, six parameters are required to define uniquely $T_{f,\max}$, $\Gamma_{\text{vib}}$, and $E_{\text{vib}}$. Measuring $T_{f,\max}$ and $\Gamma_{\text{vib}}$ for one structure does not determine the parameters of the barriers. Conversely, without information on the barrier parameters, $T_{f,\max}$ and $\Gamma_{\text{vib}}$ can be chosen independently of each other. Solving the wave equation produces similar results as long as the trapped level is well below the height of the lower barrier. Therefore, to calculate a maximum resonance area, we can set $T_{f,\max} = 1$ (ignoring the dependence of the fission penetrability on the fission barrier shape).

#### 5. *$f^{KJ}(\alpha)$ functions*

If we assume that the fission fragments are emitted along the axis of symmetry of the nucleus and that $K$ is a good quantum number from the transition state to scission, then the directional dependence of the fragments is determined uniquely by the quantum numbers, $J$, $K$, and $M$ (the projection of $J$ onto the space-fixed axis, normally taken to be the direction of the incoming projectile). The probability that a transition state defined by $J, K, M$ emits a fragment at an angle $\alpha$ relative to the beam direction into a conical volume defined by the angular increment $d\alpha$ is given by[33]

$$dP^{KJM}(\alpha) = \frac{2J+1}{4\pi} \left| d^J_{MK}(\alpha) \right|^2 d\Omega , \qquad (11)$$

where $\left| d^J_{MK}(\alpha) \right|$ is the absolute value of the angular part of the wave function of the Hamiltonian for a rigid rotor.[34] The angular distribution of the fission fragments is given by $dP^{KJM}/d\Omega$ and is normalized so that

$$\int_0^{\pi} \frac{2J+1}{2} \left| d^J_{MK}(\alpha) \right|^2 \sin\alpha\, d\alpha = 1 .$$

In general, both $\pm K$ projections contribute equally to the distribution. In addition, for unaligned nuclei and for even targets, all projections of $M$ carry equal weights. Therefore, the distribution must be averaged over $\pm K$ and summed over all allowed values of $M$

$$\tfrac{1}{2} \sum_{M=-m_0}^{m_0} \frac{dP^{KJM}}{d\Omega}(\alpha) + \frac{dP^{-KJM}}{d\Omega}(\alpha) = \frac{2J+1}{8\pi} \sum_{M=m_0}^{m_0} \left| d^J_{MK}(\alpha) \right|^2 + \left| d^J_{M-K}(\alpha) \right|^2 , \qquad (12)$$

where $m_0$ is the minimum value of $(J, I+\frac{1}{2})$ and $I$ is the target spin.

For an even target $m_0=\frac{1}{2}$, Eq. (12) can be simplified to

$$\frac{2J+1}{4\pi}\left[\left|d^J_{1/2,K}(\alpha)\right|^2+\left|d^J_{1/2,-K}(\alpha)\right|^2\right]. \quad (13)$$

And finally, multiplying Eq. (13) by $2\pi$ we arrive at the expression for the $f$ function

$$f^{KJ}(\alpha)=\frac{2J+1}{2}\left[\left|d^J_{1/2,K}(\alpha)\right|^2+\left|d^J_{1/2,-K}(\alpha)\right|^2\right]. \quad (14)$$

To reduce our data to cross section and to calculate theoretical cross sections for a specific $K, J$, we need to evaluate integrals of $f^{KJ}(\alpha)$ over the geometry of the grid in the chamber. Rather than deal with the $d$ functions directly, we algebraically reduce Eq. (14) to a polynomial in even powers of $\mu=\cos\alpha$,

$$f^{KJ}(\alpha)=c^{KJ}\sum_{n=0}^{4}a_n^{KJ}\mu^{2n}. \quad (15)$$

Values of the coefficients $a_n^{KJ}$ and $c^{KJ}$ for $\frac{1}{2}\leq K$, $J\leq\frac{9}{2}$ are listed in Table II. Equation (15) is normalized so that for a plane source $\int_0^1 f(\alpha)d\mu=1$. The range on $J$, and therefore $K$, corresponds to a range on the neutron orbital angular momentum of $0\leq l\leq 4$. Values of $l>4$ make a negligible contribution to the cross section in the energy region of greatest interest in $^{232}$Th, namely, $E_n<3$ MeV.

### 6. $W_t^{KJ}(i)$ integrals

These integrals depend on the angular momentum quantum numbers $K, J$ through the functions $f^{KJ}(\alpha)$ defined in Sec. V C 5 and can be written as

$$W_t^{KJ}(i)=\frac{c^{KJ}}{\pi P^2}\int_0^P\int_0^{2\pi}\int_{\theta_L(i)}^{\theta_U(i)}\int_{r_L(i,\theta)}^{r_U(i,\theta)}\sum_{n=0}^{4}a_n^{KJ}\cos^{2n+1}\alpha\; r\rho\, dr\, d\theta\, d\phi\, d\rho, \quad (16)$$

where the deposit is defined by the coordinates $\rho, \phi$, and the geometry of the grid by the coordinates $r, \theta$. Explicit expressions for $\theta_{L,U}(i)$, $r_{L,U}(i,\theta)$, and $\alpha$ are given in Ref. 22. Equation (16) was evaluated using numerical and Monte Carlo techniques.[22] The results of these calculations for the three grids and for all the functions of $f^{KJ}(\alpha)$ given in Table II are listed in Table III.

TABLE II. Values for the coefficients $c^{KJ}$ and $a_n^{KJ}$ in the expansion for the angular distribution of the fission fragments emitted from an even-odd transition nucleus.

| $K$ | $J$ | $c^{KJ}$ | $a_0^{KJ}$ | $a_1^{KJ}$ | $a_2^{KJ}$ | $a_3^{KJ}$ | $a_4^{KJ}$ |
|---|---|---|---|---|---|---|---|
| $\frac{1}{2}$ | $\frac{1}{2}$ | 1 | 0 | 0 | 0 | 0 | 0 |
| $\frac{1}{2}$ | $\frac{3}{2}$ | $\frac{1}{2}$ | 1 | 3 | 0 | 0 | 0 |
| $\frac{1}{2}$ | $\frac{5}{2}$ | $\frac{3}{4}$ | 1 | −2 | 5 | 0 | 0 |
| $\frac{1}{2}$ | $\frac{7}{2}$ | $\frac{1}{16}$ | 9 | 45 | −165 | 175 | 0 |
| $\frac{1}{2}$ | $\frac{9}{2}$ | $\frac{5}{64}$ | 9 | −36 | 294 | −644 | 441 |
| $\frac{3}{2}$ | $\frac{3}{2}$ | $\frac{3}{2}$ | 1 | −1 | 0 | 0 | 0 |
| $\frac{3}{2}$ | $\frac{5}{2}$ | $\frac{3}{8}$ | 1 | 14 | −15 | 0 | 0 |
| $\frac{3}{2}$ | $\frac{7}{2}$ | $\frac{15}{16}$ | 1 | −7 | 27 | −21 | 0 |
| $\frac{3}{2}$ | $\frac{9}{2}$ | $\frac{15}{32}$ | 1 | 20 | −126 | 252 | −147 |
| $\frac{5}{2}$ | $\frac{5}{2}$ | $\frac{15}{8}$ | 1 | −2 | 1 | 0 | 0 |
| $\frac{5}{2}$ | $\frac{7}{2}$ | $\frac{5}{16}$ | 1 | 33 | −69 | 35 | 0 |
| $\frac{5}{2}$ | $\frac{9}{2}$ | $\frac{35}{32}$ | 1 | −12 | 66 | −100 | 45 |
| $\frac{7}{2}$ | $\frac{7}{2}$ | $\frac{35}{16}$ | 1 | −3 | 3 | −1 | 0 |
| $\frac{7}{2}$ | $\frac{9}{2}$ | $\frac{35}{128}$ | 1 | 60 | −186 | 188 | −63 |
| $\frac{9}{2}$ | $\frac{9}{2}$ | $\frac{315}{128}$ | 1 | −4 | 6 | −4 | 1 |

TABLE III. Values of $W_t^{KJ}(i)$ for $i = 20°$, 30°, and 45°, and for $\frac{1}{2} \leq K,J, \leq \frac{9}{2}$.

| $K$ | $J$ | $W_t^{JK}(20°)$ (sr) | $W_t^{JK}(30°)$ (sr) | $W_t^{JK}(45°)$ (sr) |
|---|---|---|---|---|
| $\frac{1}{2}$ | $\frac{1}{2}$ | 0.0964 | 0.2330 | 0.6340 |
| $\frac{1}{2}$ | $\frac{3}{2}$ | 0.1830 | 0.4290 | 1.0850 |
| $\frac{1}{2}$ | $\frac{5}{2}$ | 0.2670 | 0.5880 | 1.3040 |
| $\frac{1}{2}$ | $\frac{7}{2}$ | 0.3270 | 0.6760 | 1.3590 |
| $\frac{1}{2}$ | $\frac{9}{2}$ | 0.3830 | 0.7330 | 1.3730 |
| $\frac{3}{2}$ | $\frac{3}{2}$ | 0.0062 | 0.0298 | 0.1840 |
| $\frac{3}{2}$ | $\frac{5}{2}$ | 0.0225 | 0.1050 | 0.5430 |
| $\frac{3}{2}$ | $\frac{7}{2}$ | 0.0526 | 0.2140 | 0.8900 |
| $\frac{3}{2}$ | $\frac{9}{2}$ | 0.0933 | 0.3490 | 1.1010 |
| $\frac{5}{2}$ | $\frac{5}{2}$ | 0.0005 | 0.0050 | 0.0680 |
| $\frac{5}{2}$ | $\frac{7}{2}$ | 0.0029 | 0.0250 | 0.2710 |
| $\frac{5}{2}$ | $\frac{9}{2}$ | 0.0093 | 0.0710 | 0.5630 |
| $\frac{7}{2}$ | $\frac{7}{2}$ | 0.0000 | 0.0010 | 0.0280 |
| $\frac{7}{2}$ | $\frac{9}{2}$ | 0.0004 | 0.0065 | 0.1360 |
| $\frac{9}{2}$ | $\frac{9}{2}$ | 0.0000 | 0.0002 | 0.0117 |

Because the calculation of the multiple integral for all values of $K$, $J$, and $i$ requires considerable computer time, Blons *et al.*[4] replaced the multiple integral by the single integral $W_a^{KJ}(i) = 2\pi \int_0^{\theta_m(i)} f^{KJ}(\alpha) \sin\alpha \, d\alpha$ where the geometry of the grid is contained in the parameter $\theta_m(i)$, the maximum angle of emission of the fission fragment from the deposit for grid $i$. To investigate the validity of this approach, we have evaluated both integrals for three representative distributions: an isotropic distribution, $f^{1/2,1/2}(\alpha)$, a distribution peaked at 0°, $f^{1/2,5/2}(\alpha)$, and a distribution peaked at 90°, $f^{5/2,5/2}\alpha$. The comparison is made in Table IV. The values of $W_a$ are 3 to 5 times greater than $W_t$ for the isotropic distribution and 9 to 16 times greater for the sideways-peaked distribution. In fact, the ratio $W_a/W_t$ is not the same for each grid. Therefore, any theoretical calculations of the cross section using $W_a$ instead of $W_t$ would not properly reproduce the trend in the data with angle, even if the calculations were normalized to a particular set of data.

TABLE IV. Values of $W_t^{KJ}(i)$ (calculation with complete grid geometry) and $W_a^{KJ}$ (calculation with approximate grid geometry) for an isotropic source distribution, for a distribution that peaks at 0°, and for a distribution that peaks at 90°.

| $(i)$ | $W_t^{KJ}(i)$ (sr) | $W_a^{KJ}(i)$ (sr) |
|---|---|---|
| | $KJ = \frac{1}{2}\ \frac{1}{2}$ | |
| 20° | 0.096 | 0.517 |
| 30° | 0.233 | 1.056 |
| 45° | 0.634 | 2.355 |
| | $KJ = \frac{1}{2}\ \frac{5}{2}$ | |
| 20° | 0.267 | 1.172 |
| 30° | 0.588 | 2.294 |
| 45° | 1.304 | 3.654 |
| | $KJ = \frac{5}{2}\ \frac{5}{2}$ | |
| 20° | 0.00051 | 0.0082 |
| 30° | 0.0050 | 0.0655 |
| 45° | 0.0680 | 0.6118 |

TABLE V. Values of theoretical $K$, $J$, areas $A_i^{KJ\pi}(E_n,i)$ for $i = 20°$, 30°, 45°, and 90°, $\frac{1}{2}^{\pm} \leq K$, $J^{\pi} \leq \frac{9}{2}^{\pm}$, $\Gamma_{\text{vib.}} = 10$ keV, and $T_{f,\max}^{KJ\pi} = 1$ at $E_n = 1.6$ MeV.

| $KJ\pi$ | 20° (mb keV) | 30° (mb keV) | 45° (mb keV) | 90° (mb keV) |
|---|---|---|---|---|
| $\frac{1}{2}\ \frac{1}{2}^+$ | 5.8 | 13.9 | 37.8 | 375.4 |
| $\frac{1}{2}\ \frac{3}{2}^+$ | 9.2 | 21.7 | 54.8 | 317.3 |
| $\frac{1}{2}\ \frac{5}{2}^+$ | 16.0 | 35.1 | 77.9 | 375.4 |
| $\frac{1}{2}\ \frac{7}{2}^+$ | 3.4 | 7.0 | 14.1 | 65.3 |
| $\frac{1}{2}\ \frac{9}{2}^+$ | 4.7 | 9.0 | 16.9 | 77.4 |
| $\frac{1}{2}\ \frac{1}{2}^-$ | 7.2 | 17.4 | 47.3 | 469.7 |
| $\frac{1}{2}\ \frac{3}{2}^-$ | 16.1 | 37.8 | 95.5 | 552.9 |
| $\frac{1}{2}\ \frac{5}{2}^-$ | 13.7 | 30.1 | 66.8 | 322.0 |
| $\frac{1}{2}\ \frac{7}{2}^-$ | 20.5 | 42.4 | 85.3 | 394.3 |
| $\frac{1}{2}\ \frac{9}{2}^-$ | 1.1 | 2.0 | 3.8 | 17.3 |
| $\frac{3}{2}\ \frac{3}{2}^+$ | 0.3 | 1.5 | 9.3 | 317.3 |
| $\frac{3}{2}\ \frac{5}{2}^+$ | 1.5 | 6.3 | 32.4 | 375.4 |
| $\frac{3}{2}\ \frac{7}{2}^+$ | 0.5 | 2.2 | 9.3 | 65.3 |
| $\frac{3}{2}\ \frac{9}{2}^+$ | 1.1 | 4.3 | 13.6 | 77.4 |
| $\frac{3}{2}\ \frac{3}{2}^-$ | 0.5 | 2.6 | 16.2 | 552.9 |
| $\frac{3}{2}\ \frac{5}{2}^-$ | 1.3 | 5.4 | 27.8 | 322.0 |
| $\frac{3}{2}\ \frac{7}{2}^-$ | 3.3 | 13.4 | 55.8 | 394.2 |
| $\frac{3}{2}\ \frac{9}{2}^-$ | 0.3 | 1.0 | 3.0 | 17.3 |
| $\frac{5}{2}\ \frac{5}{2}^+$ | 0.0 | 0.3 | 4.1 | 375.4 |
| $\frac{5}{2}\ \frac{7}{2}^+$ | 0.0 | 0.3 | 2.8 | 65.3 |
| $\frac{5}{2}\ \frac{9}{2}^+$ | 0.1 | 0.9 | 6.9 | 77.4 |
| $\frac{5}{2}\ \frac{5}{2}^-$ | 0.0 | 0.3 | 3.5 | 322.0 |
| $\frac{5}{2}\ \frac{7}{2}^-$ | 0.2 | 1.6 | 17.0 | 394.3 |
| $\frac{5}{2}\ \frac{9}{2}^-$ | 0.0 | 0.2 | 1.5 | 17.3 |
| $\frac{7}{2}\ \frac{7}{2}^+$ | 0.0 | 0.0 | 0.3 | 65.3 |
| $\frac{7}{2}\ \frac{9}{2}^+$ | 0.0 | 0.1 | 1.7 | 77.4 |
| $\frac{7}{2}\ \frac{7}{2}^-$ | 0.0 | 0.1 | 1.8 | 394.3 |
| $\frac{7}{2}\ \frac{9}{2}^-$ | 0.0 | 0.0 | 0.4 | 17.3 |
| $\frac{9}{2}\ \frac{9}{2}^+$ | 0.0 | 0.0 | 0.0 | 77.4 |
| $\frac{9}{2}\ \frac{9}{2}^-$ | 0.0 | 0.0 | 0.0 | 17.3 |

TABLE VI. Values of theoretical $K$-band areas $A_t^{K\pi}(E_n,i)$ for $i = 20°$, 30°, 45°, and 90°, $\frac{1}{2}^{\pm} \leq K^{\pi} \leq \frac{9}{2}^{\pm}$, $\Gamma_{vib} = 10$ keV, and $T_{f,max}^{KJ\pi} = 1$ at $E_n = 1.6$ MeV.

| $K\pi$ | 20° (mb keV) | 30° (mb keV) | 45° (mb kev) | 90° (mb keV) |
|---|---|---|---|---|
| $\frac{1}{2}^+$ | 39.1 | 86.8 | 201.6 | 1210.9 |
| $\frac{3}{2}^+$ | 3.5 | 14.3 | 64.6 | 835.5 |
| $\frac{5}{2}^+$ | 0.2 | 1.4 | 13.8 | 518.2 |
| $\frac{7}{2}^+$ | 0.0 | 0.1 | 2.0 | 142.8 |
| $\frac{9}{2}^+$ | 0.0 | 0.0 | 0.1 | 77.4 |
| $\frac{1}{2}^-$ | 58.6 | 129.7 | 298.7 | 1756.2 |
| $\frac{3}{2}^-$ | 5.4 | 22.4 | 102.9 | 1286.5 |
| $\frac{5}{2}^-$ | 0.2 | 2.0 | 22.0 | 733.6 |
| $\frac{7}{2}^-$ | 0.0 | 0.1 | 2.1 | 411.5 |
| $\frac{9}{2}^-$ | 0.0 | 0.0 | 0.0 | 17.3 |

### D. Results for the vibrational resonance areas

Theoretical values of individual resonance areas $A_t^{KJ\pi}(E,i)$ for $i = 20°$, 30°, 45°, and 90° ($\theta_m = 90°$), $\frac{1}{2}^{\pm} \leq K$, $J^{\pi} \leq \frac{9}{2}^{\pm}$, and $E_n = 1.6$ MeV are listed in Table V. In calculating these areas, we use the values of $\sigma_f^{KJ\pi}(T_{f,max} = 1)$ listed in Table I and let $\Gamma_{vib} = 10$ keV. These areas can be scaled by $T_{f,max} \times \Gamma_{vib}/10$ for other choices of $\Gamma_{vib}$ and $T_{f,max}$. The areas for complete $K$ bands,

$$A_t^{K\pi}(E_n,i) = \sum_{J \geq K}^{J \leq 9/2} A_t^{KJ\pi}(E_n,i),$$

are listed in Table VI.

Tables V and VI, for $i = 20°$ and 30°, show that the most important contribution to the area of a structure in the 1- to 2-MeV region comes from $K = \frac{1}{2}$ and $K = \frac{3}{2}$ components. The $K > \frac{3}{2}$ components are minimal even for $i = 45°$ and become important only for $i = 90°$. The gridded data ($i = 20, 30, 45°$) are most sensitive to the $K \leq \frac{3}{2}$ components.

## VI. COMPARISON OF THE EXPERIMENTAL AND THEORETICAL AREAS

### A. General

Experimental values for the areas of the structures at ~1.4, ~1.6, and ~1.7 MeV are plotted in Figs. 7–9 as a function of the angle $\theta_m$ (Fig. 2). The lower and upper limits are 1.33 and 1.5 MeV for the 1.4-MeV area; 1.5 and 1.65 MeV for the 1.6-MeV area; and 1.65 and 1.75 MeV for the 1.7-MeV area. These values represent the areas above a baseline drawn under the structures that approximates the plateau region above the fission threshold at ~1.3 MeV. The errors plotted are

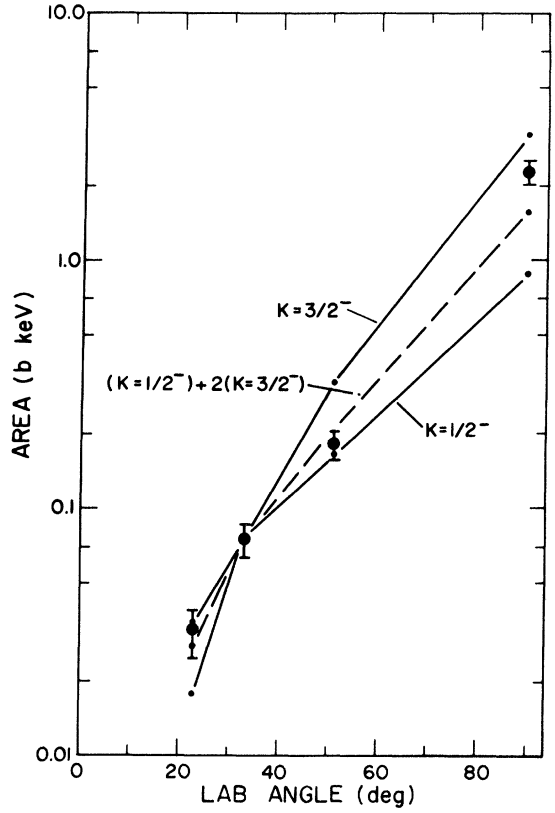


FIG. 7. Comparison of the experimental areas with theoretical predictions of complete rotational bands for the 1.4-MeV structure. The solid lines connect the theoretical areas for a $K = \frac{1}{2}^-$ band and a $K = \frac{3}{2}^-$ band. The dashed line connects the areas for the combination $(K = \frac{1}{2}^-) + 2(K = \frac{3}{2}^-)$. All curves are normalized to the experimental area at $\theta_m = 33.7°$. The predictions for the positive parity bands are similar.

conservative estimates of how accurately we can define the areas.

The solid lines in these figures represent the trend of the theoretical areas listed in Table VI with angle for complete $K=\frac{1}{2}^-$ and $K=\frac{3}{2}^-$ bands. The dashed lines in Figs. 7 and 9 represent cases for combinations of a $K=\frac{1}{2}^-$ band and a $K=\frac{3}{2}^-$ band with the weights indicated in the figures.

We have normalized the theoretical areas to the experimental areas at $\theta_m=33.7°$. We are allowed this freedom as long as the ratio of the experimental to theoretical areas times $\Gamma_{vib}$ does not exceed the minimum observed width of the structure. For instance, the theoretical areas for the 1.6-MeV structure could be increased by a factor of 5 [observed width of the structure in the 30° data (~50 keV) divided by the actual width used in Tables V and VI] before violating this constraint. However, not all members of a $K$ band could have a width of 50 keV and still preserve an overall width for the band of 50 keV.

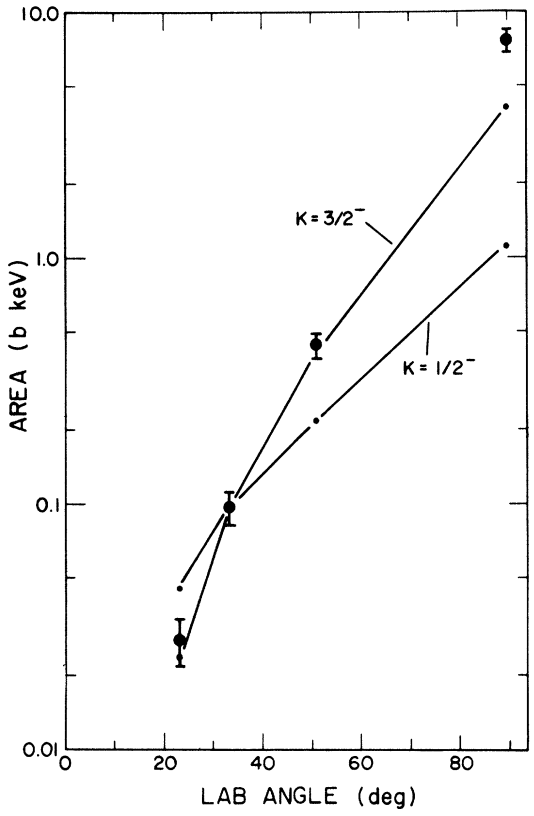


FIG. 8. Comparison of the experimental areas with theoretical predictions of complete rotational bands for the 1.6-MeV structure. The solid lines connect the theoretical areas for a $K=\frac{1}{2}^-$ band and a $K=\frac{3}{2}^-$ band. Both curves are normalized to the experimental area at $\theta_m=33.7°$. The predictions for the positive parity bands are similar.

It is possible that the structure is composed of several $K$ bands in which case the theoretical area would be a sum over these bands, and we would not necessarily have to increase $\Gamma_{vib}$ to match the experimental areas.

In the following section we do not explicitly specify the parity of the $K$ band because both parity bands give comparable results. In addition, we use the results in Tables V and VI for $E_n=1.6$ MeV and ignore the energy dependence of these quantities.

### B. Complete $K$-band area results

#### *1. 1.4-MeV structure*

For the 1.4-MeV structure, the trend in the experimental gridded areas with angle can be explained almost entirely by a $K=\frac{1}{2}$ band. However, the $K=\frac{1}{2}$ band underestimates the 90° area by about a factor of 2. This can be improved

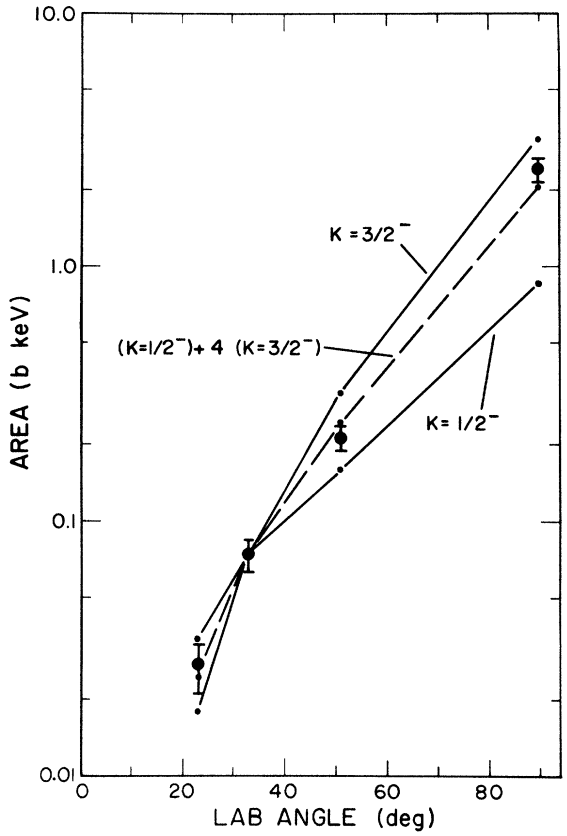


FIG. 9. Comparison of the experimental areas with theoretical predictions of complete rotational bands for the 1.7-MeV structure. The solid lines connect the theoretical areas for a $K=\frac{1}{2}^-$ band and a $K=\frac{3}{2}^-$ band. The dashed line connects the areas for the combination $(K=\frac{1}{2}^-)+4(K=\frac{3}{2}^-)$. All curves are normalized to the experimental area at $\theta_m=33.7°$. The predictions for the positive parity bands are similar.

slightly by combining a $K=\frac{3}{2}$ band with a $K=\frac{1}{2}$ band in the ratio of 2:1 as shown in Fig. 7 by the dashed line. These two bands in this ratio more than account for the observed gridded areas, which means $T_{f,\max}$ and/or $\Gamma_{vib}$ can be smaller. If we normalize the theoretical areas for these two bands with the ratio 2:1 to the 33.7° experimental area and use the ungridded area to calculate the relative fission strengths (integrated over polar angle) for $K=\frac{1}{2}$, $\frac{3}{2}$, and $\geq\frac{5}{2}$ bands, we find that they are in the proportion of 1.7:2.4:1.0. A conservative estimate of the uncertainty on these ratios is about ±15%.

#### 2. *1.6-MeV structure*

For the 1.6-MeV structure the gridded areas can be explained entirely by several $K=\frac{3}{2}$ bands, as shown in Fig. 8 by the solid line labeled $K=\frac{3}{2}$. A single $K=\frac{3}{2}$ band does not have sufficient area, even if $\Gamma_{vib}$ is greater than 10 keV, to account for the experimental gridded areas. Likewise, these bands do not account for all the 90° area; in fact, they account for only about $\frac{3}{4}$ of the area. Even if there is a significant $K=\frac{1}{2}$ component in the 1.6-MeV structure, it would not help at 90°; $A_t^{1/2}(90°) \ll A_t^{3/2}(90°)$. Therefore, we are required again to invoke $K\geq\frac{5}{2}$ components in the 1.6-MeV structure. In this case, however, the unaccounted for 90° area, about 4 bkeV, would require many $K\geq\frac{5}{2}$ bands because they have relatively weak strength at 90°. Assuming that most of the experimental area at 33.7° is a result of $K=\frac{3}{2}$ bands, the approximate relative fission strengths (integrated over polar angle) for the $K=\frac{1}{2}$, $\frac{3}{2}$, and $\geq\frac{5}{2}$ bands are in the proportion of 0.0:2.6:1.0.

#### 3. *1.7-MeV structure*

For the 1.7-MeV structure neither a $K=\frac{1}{2}$ nor a $K=\frac{3}{2}$ band accounts separately for the gridded areas. However, if we combine these bands in the ratio of $4(K=\frac{3}{2}):(K=\frac{1}{2})$, then we can fit rather well all experimental areas, even the 90° area, as indicated by the dashed line in Fig. 9. The sum of the theoretical areas for these two bands more than accounts for all experimental areas, again suggesting smaller values for $T_{f,\max}$ and/or $\Gamma_{vib}$. Using the 4:1 ratio for the $K=\frac{3}{2}$ to $K=\frac{1}{2}$ strengths normalized to the experimental area at 33.7°, the approximate relative fission strengths (integrated over polar angle) for the $K=\frac{1}{2}$, $\frac{3}{2}$, and $\geq\frac{5}{2}$ bands are in the proportion of 1.0:2.8:0.0.

### C. Individual $K,J$ area results

So far, we have tried to explain the observed areas in terms of complete $K$ bands in which each rotational member has the same $T_{f,\max}$ and $\Gamma_{vib}$ parameters. This is probably an oversimplification. It is more likely that the fission barrier parameters of individual states are different from each other, and that not all members of a particular $K$ band would have sufficient strength to be observed in the data. An analysis in terms of individual resonance with parameters unrelated to each other except in some average sense would be unmanageable without additional data and, therefore, any result would not be very meaningful. It is worthwhile, however, to mention two general observations based on the data in Table V and the experimental areas. Let us concentrate on the 1.6-MeV structure because it is defined better in the gridded data than the other structures. The experimental area of the 30° structure is about 97 mbkeV. An inspection of the $K=\frac{3}{2}$ areas in Table V reveals that no single resonance would exhaust this area even if $\Gamma_{vib}$ is increased to the observed width of ~50 keV; for the 1.6-MeV structure, many $K=\frac{3}{2}$ resonances are required. In addition, the $K=\frac{3}{2}$ areas would underestimate the experimental 90° area, thus requiring $K\geq\frac{5}{2}$ components. A similar statement can be made for the other two structures, namely, that many individual resonances are required for each structure, and except for possibly the 1.7-MeV structure, $K\geq\frac{5}{2}$ components are present in the structures.

## VII. COMPARISON WITH DOUBLE- AND TRIPLE-HUMPED BARRIER CALCULATIONS

Two attempts have been made at a detailed channel analysis of the structure in $^{233}$Th in the 1- to 2-MeV neutron-energy region using fission cross-section and angular distribution or anisotropy data. Caruana *et al.*[18] compare the results from a triple-humped model with those from a double-humped model by fitting their angular distribution data and the fission cross-section data of Blons *et al.*[4] For the double-humped model, they cannot fit both data sets with the same set of $K$-band parameters, even after an extensive trial-and-error search of many different sets. For the triple-humped model, both data sets in the region of the 1.6- and 1.7-MeV structures can be described adequately by either the set (1) $K=\frac{1}{2}^+, \frac{5}{2}^-$ (1.4 MeV), $\frac{3}{2}^+, \frac{3}{2}^-, \frac{5}{2}^-$ (1.6 MeV), and $\frac{1}{2}^+, \frac{5}{2}^+$ (1.7 MeV), or the set (2) $K=\frac{3}{2}^+, \frac{1}{2}^+$ (1.4 MeV), $\frac{5}{2}^-, \frac{3}{2}^-, \frac{3}{2}^-, \frac{5}{2}^-$ (1.6 MeV), and $\frac{5}{2}^+, \frac{1}{2}^+$ (1.7 MeV). The energy in parentheses indicates the structures to which the preceding $K$ bands apply. However, neither triple-humped set gives a satisfactory fit to the 1.4-MeV region, although set (2), which has $K=\frac{3}{2}$ and $\frac{1}{2}$ components, gives a better fit to their 1.35-MeV angular distribution.

Table VII. Transition state parameters ($K\pi, \Gamma_{vib}, T_{f,max}$) for the structures at ~1.4, ~1.6, and ~1.7 MeV in $^{233}$Th.[a]

| Structure (MeV) | $K\pi$ | $\Gamma_{vib}$ (keV) | $T_{f,max}$ |
|---|---|---|---|
| 1.4 | $\frac{1}{2}^+$ | 75 | 0.29 |
| | $\frac{3}{2}^+$ | 80 | 0.53 |
| 1.6 | $\frac{1}{2}^+$ | 107 | 0.11 |
| | $\frac{3}{2}^+$ | 82 | 0.42 |
| | $\frac{3}{2}^\pm$ | 53 | 0.60 |
| | $\frac{5}{2}^\pm$ | 83 | 0.49 |
| 1.7 | $\frac{1}{2}^\pm$ | 47 | 0.10 |
| | $\frac{3}{2}^+$ | 42 | 0.40 |

[a]Based on the barrier parameters of Abou Yehia *et al.* (Ref. 24).

In general, set (2) agrees better than set (1) with our results, although we require $K=\frac{3}{2}$ components for the 1.7-MeV structure, and most certainly, $K\geq\frac{5}{2}$ components for the 1.4-MeV structure.

A significantly better fit to the fission cross section and to all $I(0°)/I(90°)$ data is obtained by Abou Yehia *et al.*[24] for a double-humped model with the transition states listed in Table VII. The values of $\Gamma_{vib}$ and $T_{f,max}$ are calculated from their barrier parameters using Eqs. (10a)–(10d). If we assume that our values of $\sigma_f$ are about the same as those used in the analysis in Ref. 24 and that $T_N + T_\gamma \gg T_f$ [consequently their areas are equal to our areas (Tables V and VI) multiplied by $\Gamma_{vib} \times T_{f,max}/10$], then their predictions about the relative strengths of the $K$ bands are in remarkable agreement with our results, particularly for the 1.7-MeV structure. Their ratio of $(K=\frac{3}{2}):(K=\frac{1}{2})$ for the 1.7-MeV structure is 3.6, and we estimated about 4. For the 1.4-MeV structure, their values for $\Gamma_{vib} \times T_{f,max}$ give 1.95 for the ratio $(K=\frac{3}{2}):(K=\frac{1}{2})$. This is the source of the factor of 2 for the dashed line in Fig. 7. And, for the 1.6-MeV structure, their parameters support our conclusion that very little $K=\frac{1}{2}$ component is required to account for the areas at all angles.

## VIII. SUMMARY

We now know from all analyses what the primary $K$ components of the fission strength of the structures are at ~1.4, ~1.6, and ~1.7 MeV in $^{233}$Th. From our results we can give the relative strengths of the $K$ components in each structure. We find the approximate proportion of $K=\frac{1}{2}$ to $K=\frac{3}{2}$ to $K\geq\frac{5}{2}$ strengths in the ratio of 1.7 : 2.4 : 1.0, 0.0 : 2.6 : 1.0, and 1.0 : 2.8 : 0.0 for the three structures, respectively. Furthermore, if the fine structure has a width of about 10 keV (with a limit of $<50$ keV) then a very large number of states are required to account for the area of each structure in the fission cross section.

And finally, because our $K$-component strengths are derived without assuming a particular fission barrier shape, they do not confirm the existence of the shallow mass-asymmetric well predicted by Möller and Nix[6] even though they are consistent with recent triple-humped barrier calculations.

## ACKNOWLEDGMENTS

We would like to express our thanks to W. A. Teasdale, J. M. Anaya, and C. E. Ragan for their assistance during the initial phases of the experiment and to J. Craven (ORELA staff) for writing the data-acquisition program and for help with computer-related problems. This work was performed under the auspices of the U. S. Department of Energy under Contract No. W-7405-ENG-36 and W-7405-ENG-26.

[1]D. W. Muir and L. R. Veeser in *Proceedings of the Third Conference on Neutron Cross Sections and Technology, Knoxville, Tennessee, 1971,* edited by R. L. Macklin (USAEC, Division of Technical Information Extension, Oak Ridge, Tennessee, 1971), pp. 292–298.

[2]S. Plattard, G. F. Auchampaugh, N. W. Hill, G. de Saussure, R. B. Perez, and J. A. Harvey, *Proceedings of Nuclear Cross Sections for Technology, Knoxville,*

*Tennessee, 1980*, edited by J. L. Fowler, C. H. Johnson, and C. D. Bowman (U. S. Government Printing Office, Washington, D.C., 1980), pp. 491–495.
[3]J. Blons, C. Mazur, D. Paya, M. Ribrag, and H. Weigmann, Phys. Rev. Lett. 41, 1282 (1978).
[4]J. Blons, C. Mazur, and D. Paya, Phys. Rev. Lett. 35, 1749 (1975).
[5]P. Möller, Nucl. Phys. A192, 529 (1972).
[6]P. Möller and J. R. Nix, Nucl. Phys. A281, 354 (1972).
[7]J. Blons, C. Mazur, D. Paya, M. Ribrag, and H. Weigmann, paper delivered at XVIII International Winter Meeting on Nuclear Physics, Bormio, Italy, 1980.
[8]J. W. Boldeman, D. Gogny, A. R. de L. Musgrove, and R. L. Walsh, Phys. Rev. C 22, 627 (1980).
[9]A. Sobiczewski, S. Bjornholm, and K. Pomorski, Nucl. Phys. A202, 274 (1973).
[10]J. Specht, J. Weber, E. Konechy, and D. Heunemann, Phys. Lett. 41B, 43 (1972).
[11]H. Backe, L. Richter, D. Habs, V. Metag, J. Pederson, P. Singer, and H. J. Specht, Phys. Rev. Lett. 42, 490 (1979).
[12]S. Bjornholm and J. E. Lynn, Rev. Mod. Phys. 52, 725 (1980).
[13]A. Sicre, Ph.D. thesis, University of Bordeaux, Report No. CENBG 7603, 1976.
[14]P. E. Vorotnikov, S. M. Dobrovina, G. A. Otroshchenco, and V. A. Shigin, Yad. Fiz. 10, 488 (1969) [Sov. J. Nucl. Phys. 10, 280 (1970)].
[15]G. D. James, J. E. Lynn, and L. G. Earwaker, Nucl. Phys. A189, 225 (1972).
[16]G. Yuen, G. T. Rizzo, A. N. Behkami, and J. R. Huizenga, Nucl. Phys. A171 614 (1971).
[17]L. R. Veeser and D. W. Muir (private communication).
[18]J. Caruana, J. W. Boldeman, and R. L. Walsh, Nucl. Phys. A285, 205 (1977).
[19]S. B. Earmagambetov and G. N. Smirenkin, Yad. Fiz. 11, 1164 (1970) [Sov. J. Nucl. Phys. 11, 646 (1970)].
[20]J. W. Behrens, Phys. Rev. Lett. 39, 68 (1977).
[21]S. Lo Nigro and C. Milone, Nucl. Phys. A96, 617 (1967).
[22]G. F. Auchampaugh, S. Plattard, N. W. Hill, G. de Saussure, R. B. Perez, and J. A. Harvey, Los Alamos Scientific Laboratory Report No. LA-8671, 1980.
[23]S. Kahn, R. Harman, and V. Forque, Nucl. Sci. Eng. 23, 8 (1965).
[24]H. Abou Yehia, J. Jary, J. Trochon, J. W. Boldemann, and A. R. de L. Musgrove, in *Proceedings on Nuclear Cross Sections for Technology, Knoxville, Tennessee, 1980*, edited by J. L. Fowler, C. H. Johnson, and D. C. Bowman (U. S. Government Printing Office, Washington, D.C., 1980), pp. 469–474.
[25]W. Hauser and H. Feshbach, Phys. Rev. 87, 366 (1952).
[26]P. A. Moldauer, Phys. Rev. 157, 907 (1967).
[27]J. E. Lynn, Atomic Energy Research Establishment, Harwell, Oxfordshire, Report No. AERE-R7468, 1974.
[28]S. F. Mughabghab and D. I. Garber, Brookhaven National Laboratory Report No. BNL-325 (National Technical Information Service, 1973), 3rd ed., Vol. 1.
[29]A. Gilbert and A. G. W. Cameron, Can. J. Phys. 43, 1446 (1965).
[30]Nucl. Data Sheets 20, 165 (1977).
[31]J. D. Cramer and J. R. Nix, Phys. Rev. C 2, 1048 (1970).
[32]E. V. Gai, A. V. Ignatiuk, N. S. Rabotnov, and G. N. Smirenkin, Los Alamos Scientific Laboratory Translation LA-4386-TR, 1971, translated by A. Vakar from paper IAEA/SM/122/132, International Atomic Energy Agency, Second Symposium on the Physics and Chemistry of Fission Processes, Vienna, 1969.
[33]J. A. Wheeler in *Fast Neutron Physics, Part II*, edited by J. B. Marion and J. L. Fowler (Interscience, New York, 1963), Chap. V. S., pp. 2051.
[34]R. W. Lamphere, Nucl. Phys. 38, 561 (1962).